

Fabrication and strengthening mechanism of crack-free nano-TiC reinforced IN738LC with enhanced mechanical properties by laser powder bed fusion.

SHU, Chang, CHEN, Siyuan, ZHENG, Zhiyu, LU, Xuben, LI, Weining, DE LISI, Michele, BIDARE, Prveen, SHU, Xuedao <<http://orcid.org/0000-0001-9928-7344>> and ESSA, Khamis <<http://orcid.org/0000-0001-6090-0869>>

Available from Sheffield Hallam University Research Archive (SHURA) at:

<http://shura.shu.ac.uk/32668/>

This document is the author deposited version. You are advised to consult the publisher's version if you wish to cite from it.

Published version

SHU, Chang, CHEN, Siyuan, ZHENG, Zhiyu, LU, Xuben, LI, Weining, DE LISI, Michele, BIDARE, Prveen, SHU, Xuedao and ESSA, Khamis (2023). Fabrication and strengthening mechanism of crack-free nano-TiC reinforced IN738LC with enhanced mechanical properties by laser powder bed fusion. *Journal of Materials Research and Technology*, 27, 3835-3848.

Copyright and re-use policy

See <http://shura.shu.ac.uk/information.html>

Fabrication and strengthening mechanism of crack-free nano-TiC reinforced IN738LC with enhanced mechanical properties by laser powder bed fusion

Chang Shu^{1*}, Siyuan Chen^{2,3}, Zhiyu Zheng^{2,3}, Xuben Lu^{2,3}, Weining Li¹, Michele De Lisi¹, Prveen Bidare^{1,4}, Xuedao Shu^{2,3}, Khamis Essa^{1*}

1 Department of Mechanical Engineering, University of Birmingham, Birmingham, B15 2TT, UK

2 Faculty of Mechanical Engineering and Mechanics, Ningbo University, Ningbo, 315211, China

3 Zhejiang Key Laboratory of Part Rolling Forming Technology, Ningbo University, Ningbo, 315211, China

4 Department of Engineering and Mathematics, Sheffield Hallam University, Sheffield, S1 1WB, UK

* Corresponding author

Abstract:

IN738LC alloy has broad application potential in modern aerospace and energy industries due to its excellent high-temperature durability, excellent corrosion and fatigue resistance, however, its application has been greatly limited due to its high crack sensitivity. To address this challenge, this research proposes a method of incorporating TiC nanoparticles to mitigate cracks and enhance the strength of the nickel-based materials. The crack-free TiC-IN738LC materials were successfully fabricated using laser-powder bed fusion. The relationship between the processing parameters and processed quality was studied. The fracture morphology and mechanical properties of samples were analyzed and the strengthening mechanisms of nano-TiC particles were clarified. The results showed that volume energy density (VED) = 111.1 J/mm³ is the optimal processing parameter with the laser energy 225W, scanning speed 750mm/s, and 0.09mm hatch distance. The effects of processing parameters were discussed in depth. Compared with the virgin IN738LC, the microhardness of TiC-IN738LC is improved by 20% to 40%, and the tensile strength of TiC-IN738LC is enhanced by 5%-30%, respectively, which indicates the significant strengthening effect of nano-TiC on IN738LC. The synergistic effect of fine grain strengthening, load-bearing strengthening and Orowan strengthening mechanisms was accounted for the performance enhancement. The research results provide an experimental reference for selecting the processing parameters of TiC-IN738LC.

Keywords:

Nanoparticles, IN738LC, Laser-powder bed fusion, Mechanical properties, Strengthening mechanism

1. Introduction

Additive manufacturing (AM) is a transformative manufacturing technology that rapidly developed in the past 30 years. Laser-powder bed fusion (L-PBF) has a high cooling rate (about 10^4 - 10^6 °C/s), and via layer-by-layer deposition and laser-induced non-equilibrium cooling and solidification process, a finer microstructure will be generated [1-4]. Studies have shown that L-PBF is an effective method for fabricating geometrically complex metal components that offer high mechanical performance [1-3, 5-7]. Given its promising capabilities, L-PBF has been widely used in numerous applications, including aviation, aerospace, biomedical sensors, and deep-sea explorations [8]. Metal matrix composites are also popular in sectors such as aviation, aerospace, biomedical sensors, deep-sea explorations, and energy industries, owing to their multi-functional properties. Currently, the production of high-quality composite materials using L-PBF is an area of active research.

Due to the high volume fraction of Ni₃(Al,Ti)- γ' , the hard-to-weld nickel superalloy IN738LC boasts a range of exceptional properties, such as high-temperature performance, creep resistance, hot corrosion, and oxidation resistance. IN738LC is a staple in modern aerospace and energy industries [1, 9, 10]. Using the L-PBF method to produce IN738LC paves the way for its expanded application in diverse sectors. Wang et al. [8] examined the processing parameters of IN738LC in L-PBF and successfully achieved IN738LC with high density, minimal porosity, and a reduced crack rate, thereby establishing the optimal processing parameter window for IN738LC. Nonetheless, hot cracking remains a significant challenge when working with hard-to-machine nickel superalloys. Identifying strategies to mitigate hot cracking is a primary research objective in the field.

To enhance the γ' precipitation strength of nickel superalloys, incorporating nanoparticles with high modulus and outstanding heat resistance is considered an effective approach to improve their properties and reduce cracking [11-13]. Wang et al. [12] integrated TiC into nickel superalloy GTD222, not only effectively suppressing cracks but also enhancing mechanical properties. Lv et al. [9] improved the mechanical attributes of CM247LC by introducing 1wt% TiC. The strengthening mechanism imparted by nanoparticles was elucidated through microscopic data analysis. Many studies have illustrated the strengthening mechanism of ceramic particles as reinforcements. The primary strengthening mechanisms encompass Orowan strengthening, fine grain strengthening, load-bearing strengthening, and dislocation strengthening [9, 14-16]. However, the elucidation of these mechanisms is mostly based on nickel superalloys such as In718, In625, etc. [16-19]. For the nanoparticles reinforced hard-to-weld nickels, the mechanisms are barely discussed and there are still gaps needed to fill in.

The processing parameters play a critical role in the materials quality [7, 20]. For L-PBFed metal materials, prevalent defects, such as pores, cracks, and lack of fusion, detrimentally impact the mechanical properties of the printed sample. Hence, it's crucial to optimize processing parameters to diminish defects and uplift processed quality [7]. The statistical Design of Experiments (DoE) method is currently the main research approach to obtain the relationship between processing parameters and processed quality. Koutiri et al. [21] studied the processing parameters of L-PBFed-IN625 by DoE, and obtained the relationship with the processed quality (surface roughness, porosity rate and tensile strength). The as-printed sample with low porosity and high strength was obtained and provided a valuable processing parameter window as the reference for the future work of L-PBFed-In625. Wang et al. [8] designed L-PBFed IN738LC through full factorials DoE, obtained the relationship diagram of processing parameters, found the correlation between defects and processing parameters, and successfully fabricated the high-density (~99.76%), crack-free samples. The microstructural results and mechanical tests validated the significant improvement of the

properties. Khorasani et al. [5] studied the rheological phenomena of molten pools under different parameters, these results were consistent with the results of density and hardness. By correlating the results of processing parameters and hardness tests as well as the numerical model's validation, the mechanism of molten pool formation and processing parameters were clarified. Zhou et al. [13] successfully printed and strengthened TiC-IN738LC by using L-PBF, but this study only applied one set of processing parameters (laser power 300W, scan speed 1000mm/s, powder layer thickness 30um, hatch space 90um), the effect on other sets of parameters is not covered. Therefore, although the above research is devoted to the parameter study of Ni-superalloys, there are many blank gaps that have not been studied, especially for the processing parameter analysis of the reinforced difficult-to-machine nickel composite materials.

In this work, the difficult-to-machine nickel superalloy IN738LC was selected as the matrix and the TiC nanoparticles were used as the reinforcements to form TiC-IN738LC metal matrix composite. The processing parameters of TiC-IN738LC by L-PBF were systematically studied. The relationship between processing parameters and the properties including density, porosity, hardness, and tensile strength was revealed. By obtaining the processing parameter network diagram, the optimal parameters of L-PBFed TiC-IN738LC were achieved. Meanwhile, by the analysis of microstructural morphology and mechanical behavior, the strengthening mechanisms and the effect of nano-TiC particles in the L-PBF process were analysed.

2. Experiments

2.1 Materials

To ensure the high printing quality, spherical shape IN738LC powder (China North Industries Group Corporation Limited, China) was selected in this study, with $d_{10}=15.9$ um, $d_{50}=34.3$ um and $d_{90}=60.2$ um. The chemical composition of IN738LC is shown in Table 1. Figure 1(a) shows the morphology of IN738LC and it shows the powder with the good quality of sphericity. The 50 nm TiC with 99.5% purity (China North Industries Group Corporation Limited, China) was chosen as the ceramic reinforcement in this work. The morphology of nano-TiC is shown in Figure 1(b). A 4-planetary ball mill machine (QM-QX, Nanjing Nanda Instrument Plant, China) was used to mix the 2wt% TiC and Nickel superalloy IN738LC. During the ball mill, the Argon gas was filled as the inert gas to prevent the impurity phase that was caused from the oxidation reaction with the powders. To fully disperse and attach the nano-TiC to IN738LC, a set of parameters from ball milling are used: 4:1 ball-to-powder ratio, 200 rpm ball mill speed and 6 hours ball mill time. Figure 1(c) and (d) show the morphology of TiC-IN738LC after ball milling, and it can be seen that the nano-TiC nanoparticles were evenly distributed to the surface of IN738LC. Figures 1(e) and 1(f) displayed the EDS graphs and the presence of both Ti and Ni elements confirms that the TiC nanoparticles were uniformly dispersed around the IN738LC powders before printing.

Table 1. Chemical composition of IN738LC (wt%).

Ni	Cr	Nb	W	Mo	Ta	Ti	Al	Co	C	Sn	Mn	B	Zr
Bal	16	0.8	2.6	1.75	1.7	3.5	3.5	8.5	0.1	0.03	0.03	0.02	0.02

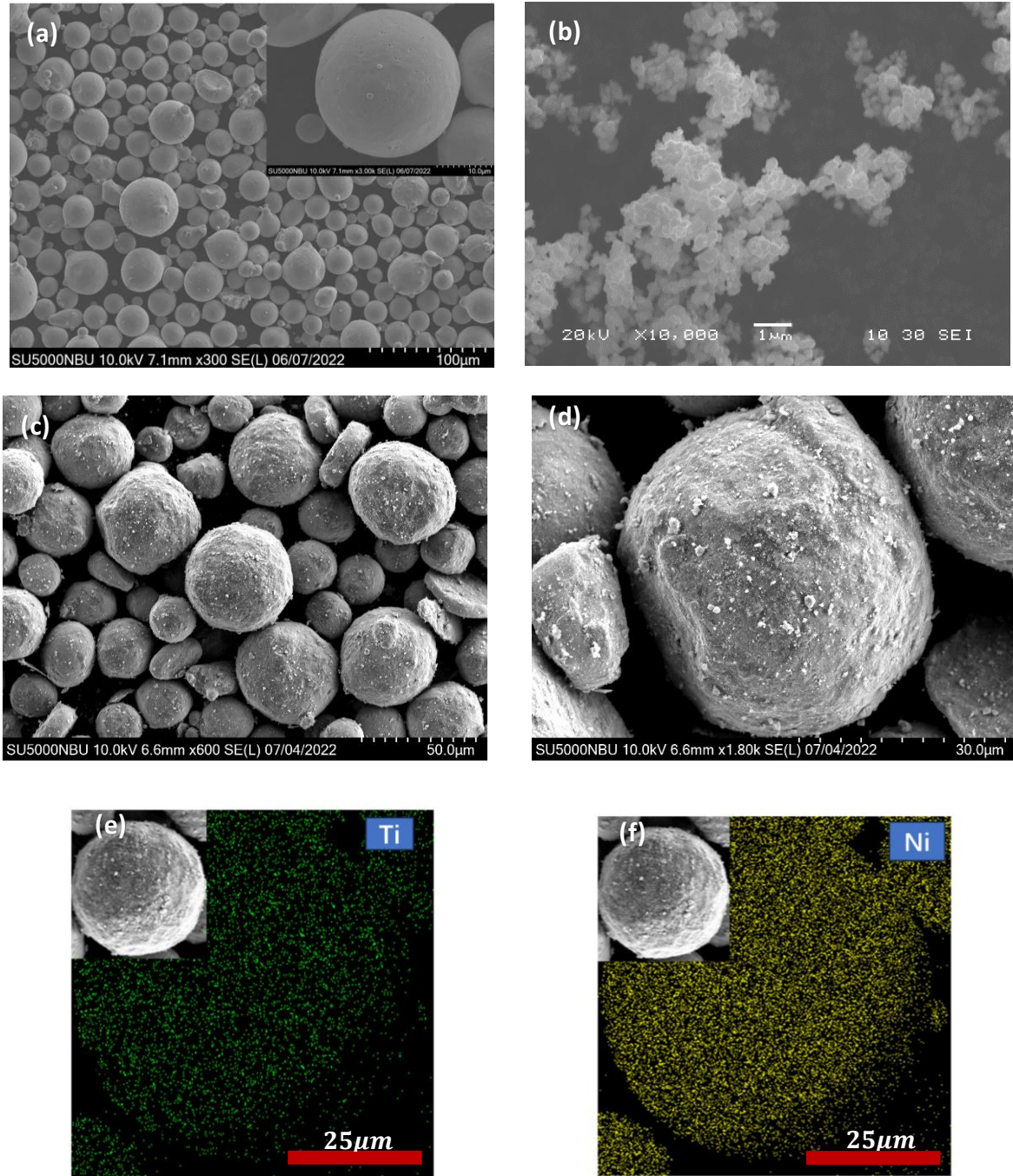


Figure 1. SEM morphology (a) IN738LC virgin powder, (b) nano-TiC powder, (c) nano-TiC attached to the IN738LC after ball milling, (d) higher magnification of the particle attachment, (e) EDS graph of Ti element and (f) EDS graph of Ni element on the prepared powder.

2.2 L-PBF process and Design of Experiment

A commercial L-PBF machine (HBD-150D, Shanghai Hanbang United 3D Tech Co., Ltd., China) was used in this work to fabricate the TiC/IN738LC. It is equipped with a 400W IPG fiber laser and a laser spot with a diameter of 70 μm. Figure 2 shows the L-PBF schematic diagram, where the cubic samples (8 mm×8 mm×8 mm) are used for the microstructural observation, and the tensile test specimen adopts the ASTM dimensions and standard [22]. Prior to the printing, the prepared powder was put into a furnace filled with inert gas and dried

for 5 hours at 40 °C. The L-PBF scanning strategy adopted the 67° rotation in the layer-by-layer scanning direction [9].

A full factorial design with three variables and three levels was used in this work. The three design variables were the laser power (150 W-300 W), scanning speed (500 mm/s-1000 mm/s) and hatch space (0.09 mm-0.12 mm). The layer thickness was set as 0.03 mm for all the trials. Table 2 shows the details of the DoE. For each set of the process parameter, it corresponds to a volume energy density (VED) value, which is generally used as an important reference to correlate the interactions between the laser source and powder[23], namely the equation (1):

$$VED = \frac{P}{vhd} \text{ (J/mm}^3\text{)} \quad (1)$$

where P , v , h and d stand for laser power, scanning speed, hatch space and layer thickness, respectively.

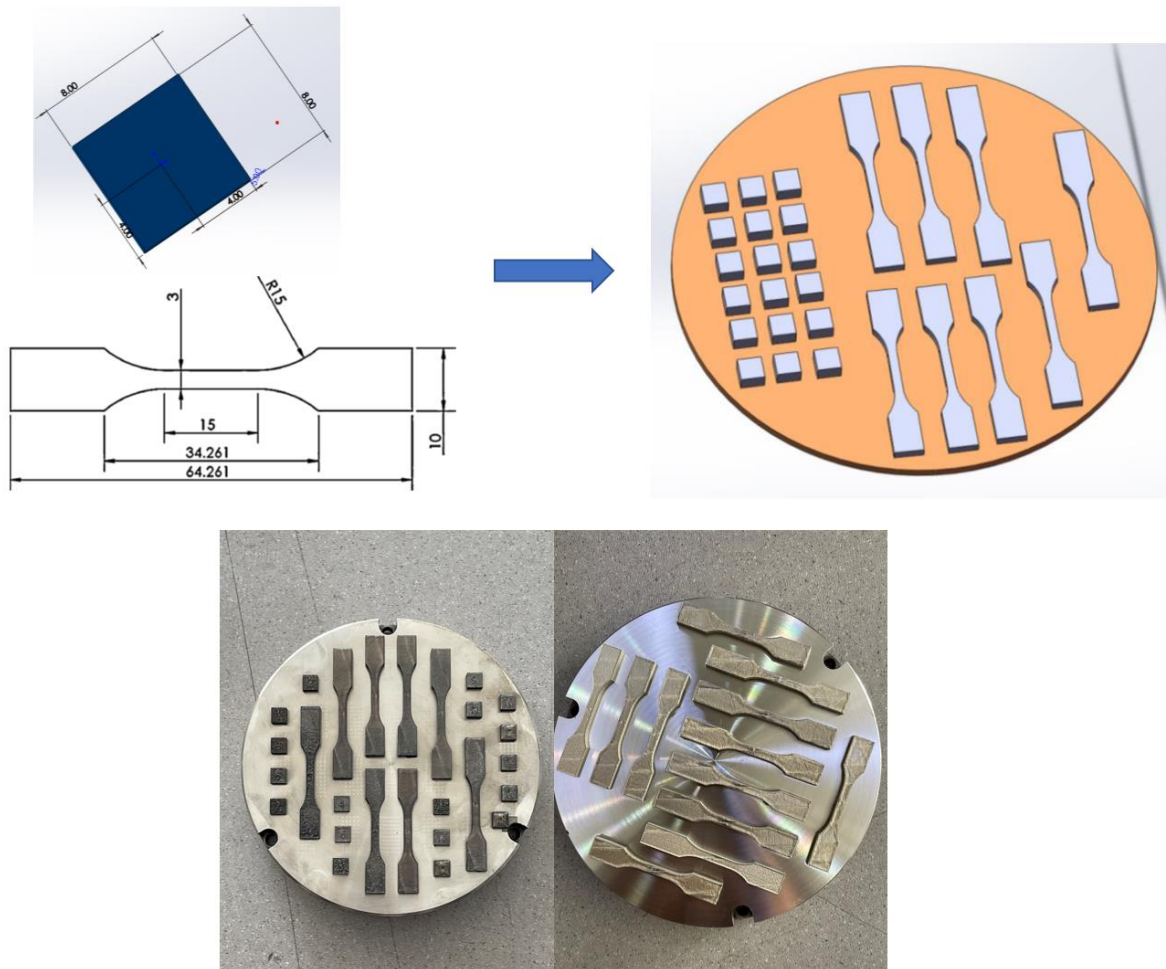


Figure 2. Schematic diagram of L-PBF process. Dimensional illustration of microstructural samples, tensile samples, and L-PBF as-printed samples.

Table 2. Design of Experiments of L-PBFed TiC-IN738LC.

# Samples	Layer thickness = 30um		
	Laser Power (W)	Scanning speed (mm/s)	Hatch space (mm)
1	150	500	0.090
2	150	500	0.105
3	150	500	0.120
4	150	750	0.090
5	150	750	0.105
6	150	750	0.120
7	150	1000	0.090
8	150	1000	0.105
9	150	1000	0.120
10	225	500	0.090
11	225	500	0.105
12	225	500	0.120
13	225	750	0.090
14	225	750	0.105
15	225	750	0.120
16	225	1000	0.090
17	225	1000	0.105
18	225	1000	0.120
19	300	500	0.090
20	300	500	0.105
21	300	500	0.120
22	300	750	0.090
23	300	750	0.105
24	300	750	0.120
25	300	1000	0.090
26	300	1000	0.105
27	300	1000	0.120

2.3 Characterization

Optical microscope (OM) was used to observe porosity as well as the melt pool morphology, and the samples should be well polished before the observations. Scanning electron microscope (SEM) (Hitachi SU5000, Japan) was used to observe the morphology of the fracture and microstructure. Before observation, the samples were ground, mounted, well-polished and etched. The samples were etched for 30 s with the selected etching solution $12\text{mlH}_3\text{PO}_4+48\text{mlH}_2\text{SO}_4+40\text{mlHNO}_3$ [13]. Electron Back Scatter Diffraction (EBSD) was acquired with 20 kV accelerating voltage and 250 nm step size.

The Archimedes principle was used to measure the density of the as-printed sample ρ_f in this work, with a high-precision (0.001g) weighing scale. The relative density was obtained by the ratio of measured sample density ρ_f to the bulk density ρ_b , where ρ_b is given from the supplier. The images collected by optical microscopy (OM) were used for the porosity and crack analysis. The build direction (BD) of cubic samples was taken as the investigated plane, and each sample collected five different regions on this plane, four of which are at the corners, and one is at the center. ImageJ, an open-source image analysis software, was used to measure porosity rate in this study. The threshold for image processing and adjustment was selected according to Reference [24], where to fix the lower limit on the pores from the segmentation, all the pores with the cubic-voxels smaller than 27 ($3\times3\times3$) are automatically neglected.

A Vickers microhardness tester (Wilson VH1102 Micro Hardness Testers, USA) was used for hardness testing in this study. The sample was well-polished to meet the criteria of the microhardness test. Two planes of the sample were used for microhardness testing, which are the building direction (BD) and scanning direction (SD). The sampling points were the straight line on the measured plane and the points were evenly taken with a distance of 0.2 mm. For each point, a 300 N load was applied with a dwell time of 10 s. The microhardness tester was calibrated before the test to ensure the accuracy of the result, and the measured systematic error was less than 0.05%. The final microhardness value was calculated by averaging at least 10 points of data on each measured plane.

A tensile machine (Zwick Amsler 100 HFT, Germany) was used for tensile testing. The tensile tests were performed at a rate of 1 mm/min, and the load direction was perpendicular to the building direction of the sample. For each parameter, three identical samples were used to perform the repeated experiments to ensure the accuracy of the results. The solution heat treatment was performed at 1120°C with accelerated air cooling and 850°C aging for 24 hours.

3. Results and Discussion

3.1 Density and porosity

Density is a frequently used metric to evaluate L-PBF as-printed samples due to its straightforward examination procedure. Multiple studies have established correlations among density, porosity, and mechanical properties [25]. Because of the inherent variations in material properties, the relationships between density and both microstructure and mechanical performance differ. Therefore, the density insights provided in this study will be valuable for future research on new composite materials.

Figure 3 illustrates the relationship between VED and density. As depicted, when the VED is low (40-80 J/mm³), the relative densities range between 80% to 90%. For VED values between 80-100 J/mm³, the relative densities notably increase to 96% to 98%. At a VED of 100-140 J/mm³, the sample density peaks, achieving high-density (>99%) as-printed samples. However, when the VED exceeds 140 J/mm³, the sample's density starts to decline, settling between 96% and 99%. It's important to highlight that the relative density at higher VED values remains substantially greater than at lower VED values. A lower VED, indicating reduced energy input, can lead to incomplete fusion and unmelted regions. This can result in the development of porous structures and cracks, thereby reducing the sample's density. Conversely, at higher VED values, excessive energy input can impact the molten pool's Marangoni effect. This can trap inert gas in the molten pool, leading to a gas trap effect, which produces fewer pores [26] and reduces relative density. To further optimize the processing parameter window, methodologies like data visualization and correlation quantification can be employed for machine learning [27], offering reliable predictions of the relationship between density and VED. Table 3 shows the results from the DoE table. In this study, the tensile samples were printed with 5 sets of parameters, which the parameters were selected according to the results of density. Overall, the density analysis shows that the VED value of 100-140 J/mm³ is the ideal processing parameter window, and the microstructural analysis in the following will further optimize the processing parameter window.

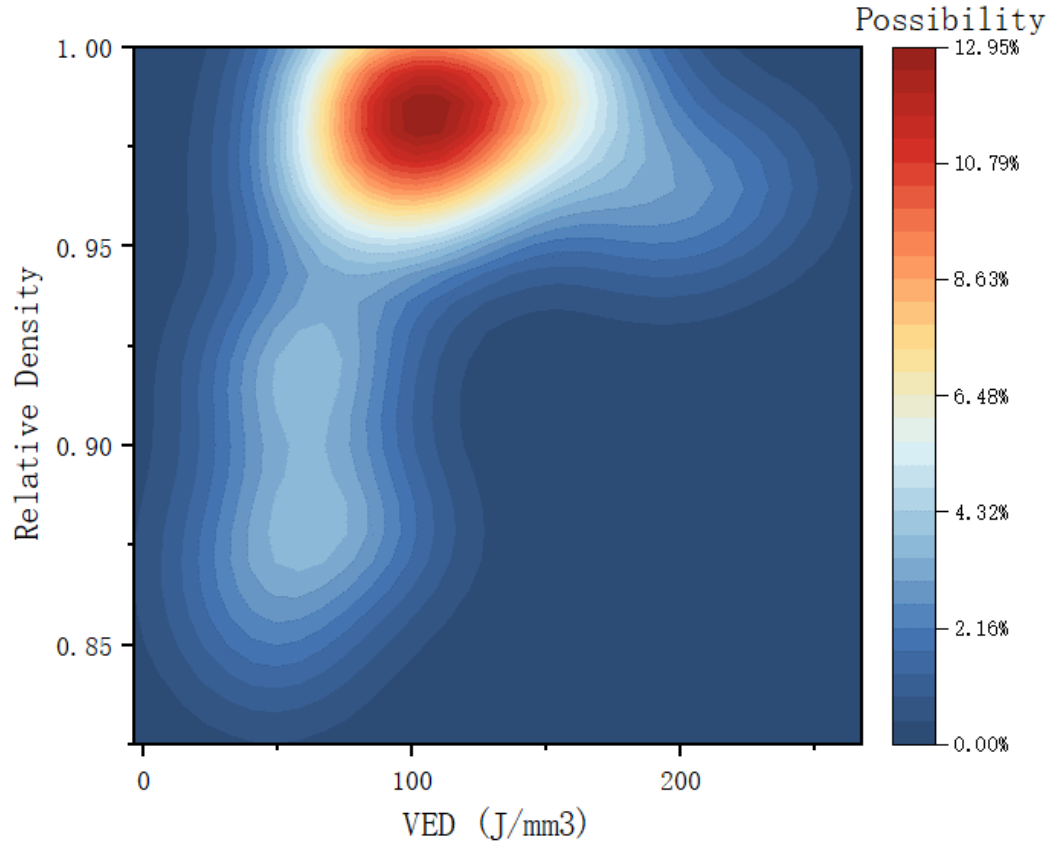


Figure 3. Relationship between VED and the relative density of as-printed samples.

Table 3. DoE table with the results of relative density and porosity.

Sample #	Laser power (W)	Scan velocity (mm/s)	Hatch space (mm)	VED (J/mm ³)	Relative density (%)	Porosity (%)
1	150	500	0.090	111.11	96.79	0.15
2	150	500	0.105	95.24	96.05	0.23
3	150	500	0.120	83.33	97.33	0.15
4	150	750	0.090	74.07	99.93	0.32
5	150	750	0.105	63.49	96.33	5.79
6	150	750	0.120	55.56	90.85	6.32
7	150	1000	0.090	55.56	92.18	0.52
8	150	1000	0.105	47.62	85.08	7.09
9	150	1000	0.120	41.67	87.29	7.52
10	225	500	0.090	166.67	97.29	0.42
11	225	500	0.105	142.86	99.86	0.26
12	225	500	0.120	125.00	96.86	1.42
13	225	750	0.090	111.11	99.02	0.17
14	225	750	0.105	95.24	99.05	0.12
15	225	750	0.120	83.33	97.08	3.17
16	225	1000	0.090	83.33	99.01	0.13
17	225	1000	0.105	71.43	92.83	0.19
18	225	1000	0.120	62.50	88.55	0.13
19	300	500	0.090	222.22	96.63	1.90

20	300	500	0.105	190.48	95.77	2.38
21	300	500	0.120	166.67	99.34	0.28
22	300	750	0.090	148.15	99.26	0.15
23	300	750	0.105	126.98	98.87	1.41
24	300	750	0.120	111.11	97.93	0.25
25	300	1000	0.090	111.11	98.79	0.15
26	300	1000	0.105	95.24	99.40	0.36
27	300	1000	0.120	83.33	87.70	0.14

Lack of fusion (LoF) and keyhole are the two main types of porosity in L-PBFed metal parts. It has been reported that the shape of pores by lack of fusion are usually in the irregular shape, with the size ranging from 10 μm to several millimeters. The lack of fusion can be attributed to insufficient penetration of the upper melt pool into the substrate or previously deposited layers [28]. Figure 4 shows the porosity graphs under each processing parameter. LoF and keyhole usually exist in samples with lower VED, for example, comparing the porosity with the laser energy of 225 W and 300 W, the laser energy of 150 W with higher scanning velocity formed more keyholes and unmelted regions, as shown in Figure 4. With the greater VED, the melting mode of the molten pool changes from the conduction mode to the keyhole mode, resulting in the molten pool forming the deep V shape [29]. If the keyhole mode is not carefully controlled, the keyhole will become unstable and repeatedly form and collapse, eventually becoming the deep spherical pores within the sample [30]. As can be seen in Figure 4, the deep spherical pores were found in samples at high VED.

Figure 5 shows the relationship between VED and porosity, and the red curve is a third-order polynomial fitting curve, which is used to represent the trend of the data and to predict the data. As evidenced by Figures 4 and 5, a noteworthy observation can be made in the context of VED ranging between 100-120 J/mm^3 . Within this spectrum, the L-PBFed TiC-IN738LC composite resulted in a considerably low porosity, below 0.3%, and a lack of cracks. This substantiates the claim that a comprehensive understanding and manipulation of processing parameters can facilitate control over crack inhibition in this innovative composite material. Meanwhile, based on the conclusion drawn from Figure 3, it agrees with the results in Figure 5, namely when the VED is within 100-140 J/mm^3 , the density is higher and the porosity is lower; when VED is less than 100 J/mm^3 or greater than 140 J/mm^3 , due to the defects such as lack of fusion and keyhole (as shown in Figure 4), the density is lower and porosity rate is higher. In summary, to achieve the prominent printability (porosity below 0.4% and crack-free) of L-PBFed samples, the optimal processing window of VED is between 100 J/mm^3 and 120 J/mm^3 .

Figure 6 shows the relationship between each processing parameter and porosity rate. Figure 6 is an important reference for determining the effect of specific parameters on porosity rate. The laser power, for instance, has a significant impact on porosity rate, with lower power levels resulting in the formation of keyholes and cracks due to the generation of LoF. Higher laser power inputs, on the other hand, provide more energy to the melt pool dynamics, particularly at lower scanning speeds and smaller hatch distances. This greater energy enables the melt pool to fully melt the powder and produce fewer LoF, resulting in a lower porosity rate. Scanning speed also affects porosity rate, with slower speeds resulting in a higher VED and a longer interaction time between the laser and powder, leading to a lower porosity rate. Conversely, faster scanning speeds reduce the interaction time, resulting in the formation of LoF. Hatch distance, which indicates the density of the neighbouring powder, also affects porosity rate, with shorter distances enabling more complete interaction between the powder and laser, resulting in a lower porosity rate. In summary, the combination of the lowest porosity rate is built under the conditions: the laser power of 225 W, scan velocity of 500 mm/s and hatch space of 0.09 mm.

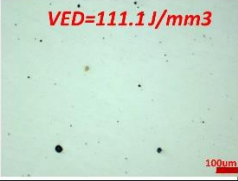
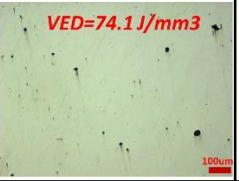
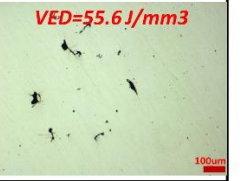




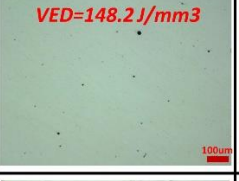

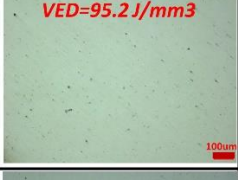
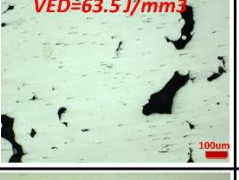
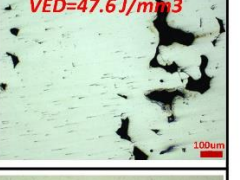
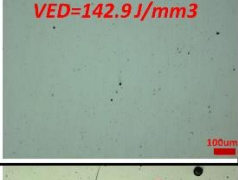

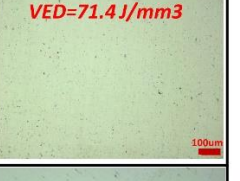


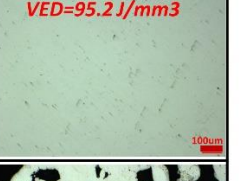
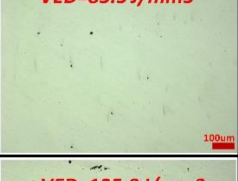
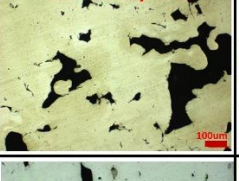
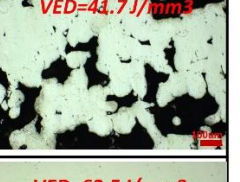
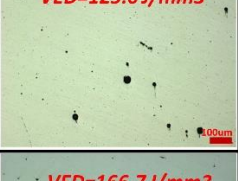
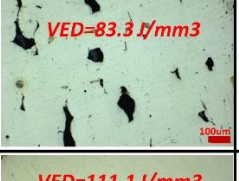
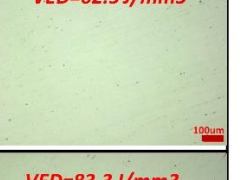



		500 mm/s	750 mm/s	1000 mm/s
$H = 0.09 \text{ mm}$	150 W	VED=111.1 J/mm³ 	VED=74.1 J/mm³ 	VED=55.6 J/mm³ 
	225 W	VED=166.7 J/mm³ 	VED=111.1 J/mm³ 	VED=83.3 J/mm³ 
	300 W	VED=222.2 J/mm³ 	VED=148.2 J/mm³ 	VED=111.1 J/mm³ 
$H = 0.105 \text{ mm}$	150 W	VED=95.2 J/mm³ 	VED=63.5 J/mm³ 	VED=47.6 J/mm³ 
	225 W	VED=142.9 J/mm³ 	VED=95.2 J/mm³ 	VED=71.4 J/mm³ 
	300 W	VED=190.5 J/mm³ 	VED=127.0 J/mm³ 	VED=95.2 J/mm³ 
$H = 0.12 \text{ mm}$	150 W	VED=83.3 J/mm³ 	VED=55.6 J/mm³ 	VED=44.7 J/mm³ 
	225 W	VED=125.0 J/mm³ 	VED=83.3 J/mm³ 	VED=62.5 J/mm³ 
	300 W	VED=166.7 J/mm³ 	VED=111.1 J/mm³ 	VED=83.3 J/mm³ 

Figure 4. Results of porosity rate under each processing parameter for all 27 L-PBFed as-printed samples. All the pictures have the same scale bar (100 μm).

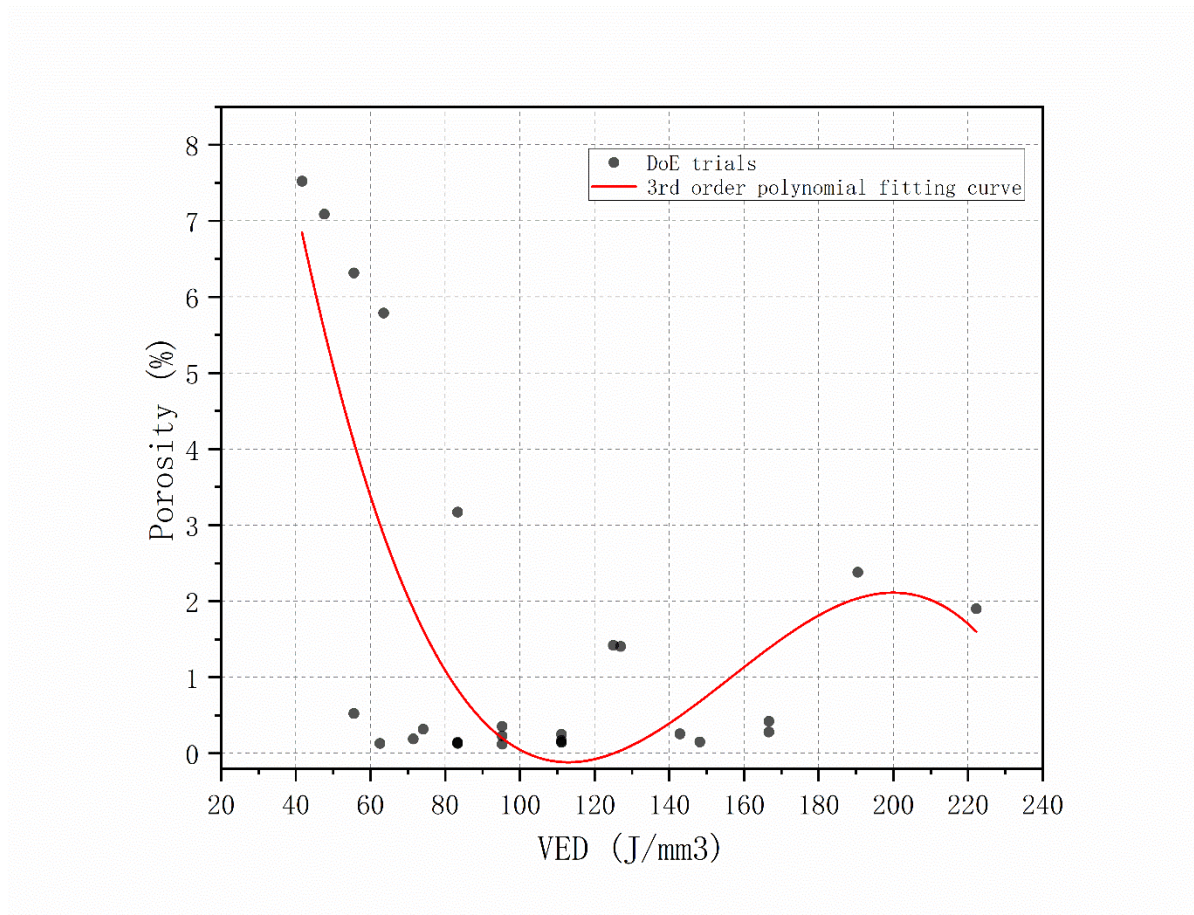


Figure 5. Relationship between VED and porosity rate of as-printed samples.

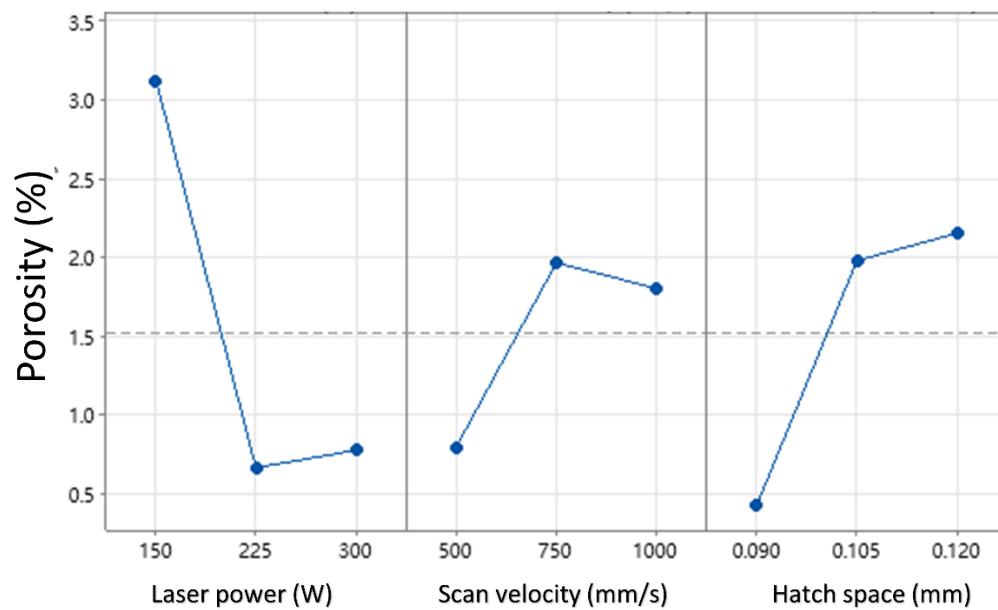


Figure 6. The relationship between porosity rate and each processing parameter.

3.2 Microhardness

A set of 7 groups of parameters were selected for the microhardness experiment based on the density and porosity results, as shown in Table 4. The results of the Vickers hardness test are shown in Figure 7. For the microhardness in the scan direction, it is obvious to find the maximum value of 625 ± 53 HV is measured at the $VED=111.1 \text{ J/mm}^3$, while the minimum value of 468 ± 50 HV is measured at $VED=74.1 \text{ J/mm}^3$. When VED continues to increase ($>111.1 \text{ J/mm}^3$), the porosity rate gradually increases due to the gas trapping effect, causing the density to decrease, and eventually lowering in the microhardness value. It is worth noting that the microhardness at low VED is much smaller than that at high VED due to the fact that cracks and keyholes are more likely to occur at low VED. For the microhardness in the build direction, the overall hardness value is smaller than that in the scanning direction, and the results follow the similar trend as the scanning direction, namely, $VED=111.1 \text{ J/mm}^3$ has the largest microhardness and the values are smaller at other VEDs. As shown in Figure 7, the overall disparity of microhardness in build direction is not as noticeable as the scanning direction. One of the reasons is that the build direction transfers more heat to the substrate or the previous layer, thus it has a more complex thermal cycle history than that in the scanning direction, thus, in building direction, the thermal gradient is larger, causing the greater residual stress and smaller microhardness[31]. According to the previous study, the high density and low porosity will contribute to the enhancement of microhardness [6], the similar conclusion has also been found in this study. In summary, the optimal microhardness was obtained at $VED=111.1 \text{ J/mm}^3$ with 527 HV in the build direction and 678 HV in the scan direction.

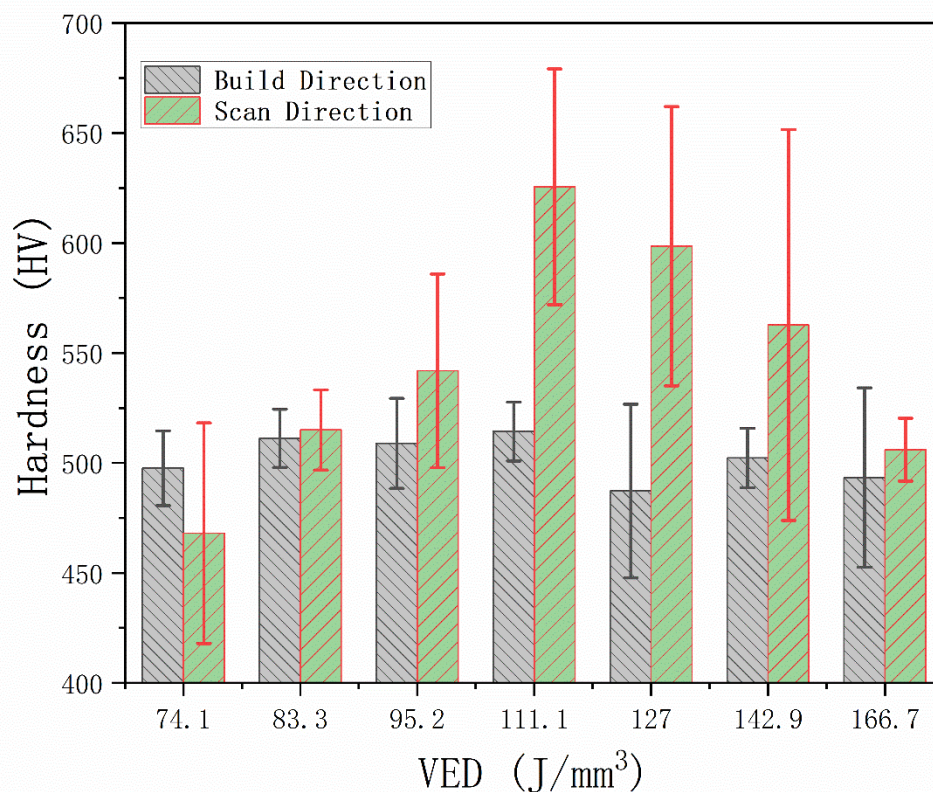


Figure 7. Microhardness results in the build directions and scan direction.

Table 4. The details of L-PBFed microhardness samples.

Sample #	Laser power (W)	Scan velocity (mm/s)	Hatch space (mm)	VED (J/mm^3)	Density (%)	Porosity (%)	BD Microhardness (HV)	SD Microhardness (HV)
1	150	750	0.090	74.1	98.93	0.32	497.6	468.0
2	225	500	0.105	142.9	99.86	0.26	502.2	562.7
3	225	750	0.090	111.1	99.02	0.17	514.2	625.8
4	225	750	0.120	83.3	97.08	3.17	511.2	515.0
5	300	500	0.120	166.7	99.34	0.28	493.3	506.0
6	300	1000	0.105	95.2	99.40	0.36	508.9	541.9
7	300	750	0.105	127.0	98.87	1.41	487.2	598.5

Figure 8 shows the comparison of microhardness between the TiC-IN738LC and IN738LC. It is obvious that TiC modified IN738LC has greater microhardness than IN738LC in both scanning direction and the building direction. In the scanning direction, the microhardness of TiC-IN738LC is about 35% higher than that of IN738LC, and about 20% higher in the building direction. For the L-PBFed IN738LC, the trend follows the similar pattern as the TiC-IN738LC, which it has the highest hardness when $\text{VED}=111.1 \text{ J}/\text{mm}^3$ or $\text{VED}=95.2 \text{ J}/\text{mm}^3$, its hardness will gradually decrease at other VEDs. For the TiC-IN738LC, due to the higher hardness of nano-ceramic particles TiC, by attaching the nanoparticles TiC to the IN738LC, several strengthening mechanisms will arise during the laser interaction. Since the nanoparticles have greater heat transfer coefficient, it will cause the thermal mismatch effect, along with the Marangoni effect of the molten pool, nanoparticles are easy to nucleate and crystallize on the grain boundary, and the slip movement along the grain boundary becomes difficult, resulting in the inhibition of dislocation, thus, enhancing its strength to resist the deformation, these strengthening mechanisms have been demonstrated and elucidated in previous studies [9, 15, 26]. It also should be noted that the previous section has shown the good attachment of TiC to IN738LC, the wetting characteristics are ensured, which is essential for printing the high-quality samples. In summary, via the addition of nanoparticles, it will cause thermal mismatch and dislocation effects, thereby the microhardness performance of TiC-IN738LC is reinforced and better than the virgin IN738LC.

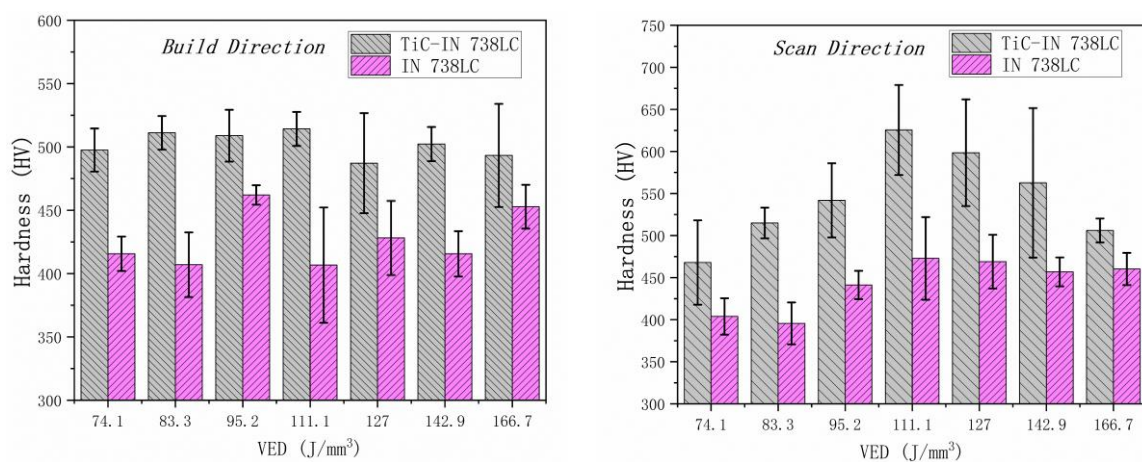


Figure 8. Microhardness comparisons between the TiC-IN738LC and IN738LC in different directions.

3.3 Tensile strength

Figure 9 shows the results of the tensile test of L-PBFed TiC-IN738LC and IN738LC and the detailed data are given in Table 5. In the tensile test of three groups of TiC-IN738LC, it can be seen that the sample at $VED=95.2 \text{ J/mm}^2$ has the largest yield stress and ultimate tensile strength, which is 9.7% and 1.4% higher than that at $VED=111.1 \text{ J/mm}^2$, and 29.7% and 19.7% higher than that at $VED=142.8 \text{ J/mm}^2$, respectively. When $VED=111.1 \text{ J/mm}^2$, the elongation rate is higher than the other two groups, which is 45.2% higher than $VED=95.2 \text{ J/mm}^2$ and 60% higher than $VED=142.8 \text{ J/mm}^2$. Overall, although the sample at $VED=111.1 \text{ J/mm}^2$ sacrifices slightly in tensile strength, the lower porosity rate, crack-free and better ductility make the $VED=111.1 \text{ J/mm}^2$ the optimal processing parameter. This work also compared the TiC-IN738LC and IN738LC in tensile tests. The IN738LC in Figure 9 adopts the optimal parameters determined in the previous research [8], and is fabricated by the same L-PBF machine in this study to ensure the consistency of the data and eliminate the potential errors between the different L-PBF machines. The ductility of IN738LC is much greater than that of TiC-IN738LC, which is 50%, 72% and 80% higher than $VED=111.1 \text{ J/mm}^2$, $VED=95.2 \text{ J/mm}^2$, and $VED=142.8 \text{ J/mm}^2$, respectively. However, the yield strength and ultimate tensile strength are much smaller than those of the nano-TiC modified IN738LC. This phenomenon widely exists in the ceramic-reinforced metal matrix composites, and the heat treatment is usually to be considered as an approach to improve the elongation [8]. Figure 10 shows the results obtained in this study compared with the previous studies on hard-to-machine Ni-superalloys [8, 32-36]. It should be noted that none of the Nickels were heat treated in Figure 10. It can be concluded from Figure 10 that the TiC-IN738LC developed in this study has significantly enhanced mechanical strength and thereby having the considerable potential value to furtherly research.

The microstructural fracture morphology reveals the fracture mechanisms in depth. Figure 11 compares the difference between brittle fracture and ductile fracture and shows clear dissimilarity of brittle and ductile fractures in the microstructures. On the surface of the brittle fracture, there are lumpy blocks, which are in the shape of regular strips. Meanwhile, the long grooves and large protrusions on the surface will significantly reduce the tensile strength. These coarse blocks and strips are less congregated than dimples (Figure. 11a, b, c) and it is easier to cause the defects and undermine ductile properties. On the other hand, there are many dimples on the ductile fracture (Figure. 11d). The deformation of the dimples can improve the plasticity of the material [37, 38]. When $VED=95.2 \text{ J/mm}^3$, the ductility of the material decreases significantly, as there are many unmelted particles and irregular blocks, which will eventually become the source of cracks and lead to the brittle fractures (Figure. 11a). In comparison, when $VED=142.8 \text{ J/mm}^3$, the fracture still has the apparent characteristics of brittle fracture, however, due to the high energy input, there is no unmelted particle found (Figure. 11c). When $VED=111.1 \text{ J/mm}^3$, there are some dimples arisen (Figure. 11b) and the ductile property is improved as shown in Figure 9. However, when comparing the fracture morphology with the IN738LC, the IN738LC has much denser dimples than TiC-IN738LC (Figure. 11d) and thereby a better ductility as presented in Figure 9. Previous studies have clarified that the ductile fracture initiates from the fracture source and rapidly propagates to the final fracture zone, however, when the protruding cracks encounter the internal micro-pores or unmelted powder, they will stop extending and lead to a clear boundary on the fracture morphology. The fibre stripes are unevenly distributed at the edge of the fracture and prone to generate the large stress concentration region, eventually leading to the ductile fracture [39]. The dimples are beneficial to the ductility but when the excessive dimples happen, it is prone to generate a larger stress concentration area and causing the strength in the tensile direction is impaired. As discussed above, the evidence of the fracture morphology agrees with the tensile test results.

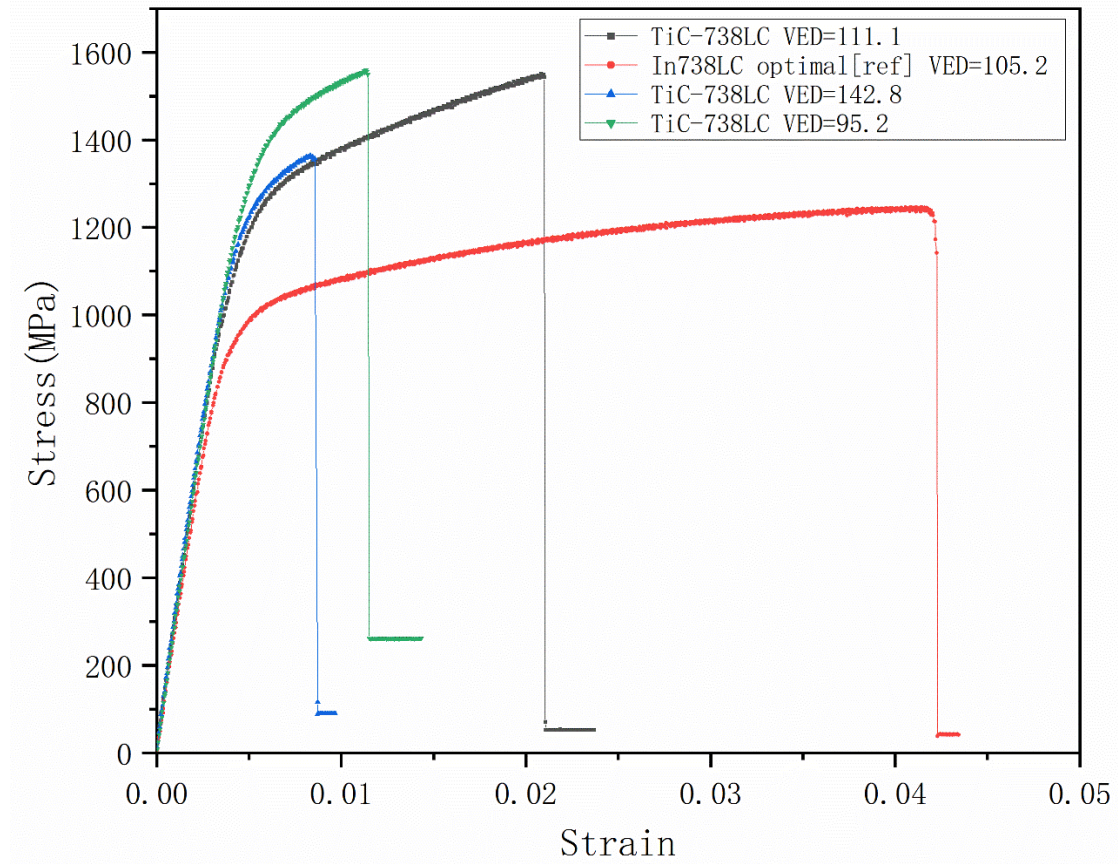


Figure 9. Tensile test results of TiC-IN738LC under different VED.

Table 5. The results of the tensile test.

Description	Yield Strength (MPa)	Ultimate Tensile Strength (MPa)	Elongation (%)
TiC-In738LC VED=111.1	1110±21	1518±12	2.1±0.05
TiC-In738LC VED=95.2	1230±33	1541±23	1.15±0.04
TiC-In738LC VED=142.8	1141±15	1321±16	0.84±0.02
In738LC VED=105.2	864±24	1238±45	4.2±0.10

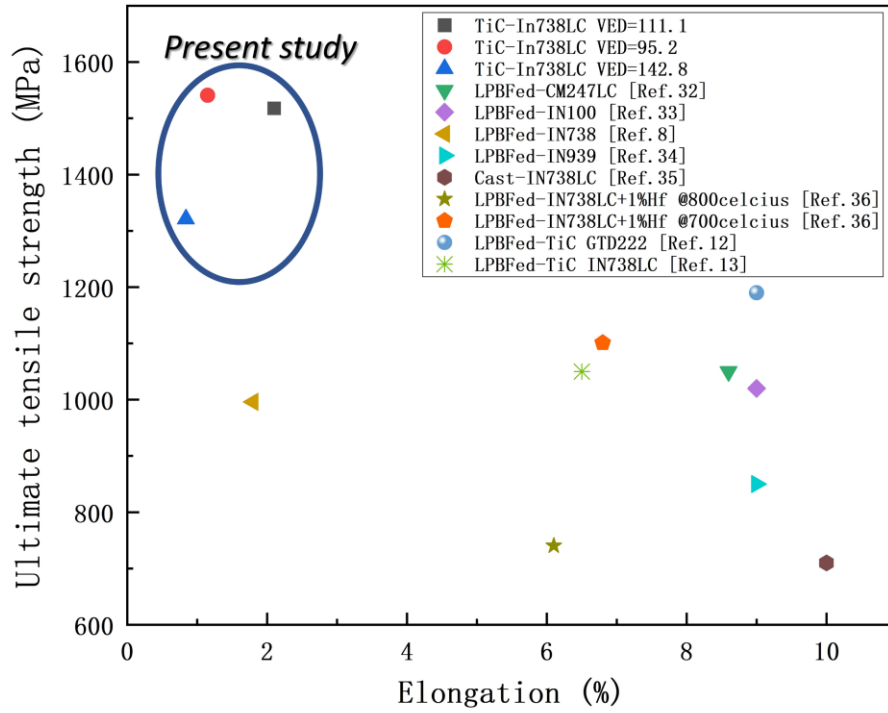


Figure 10. Comparison of elongation rate and ultimate tensile strength between this study (circled in the graph) and other difficult-to-machine nickel superalloys studies.

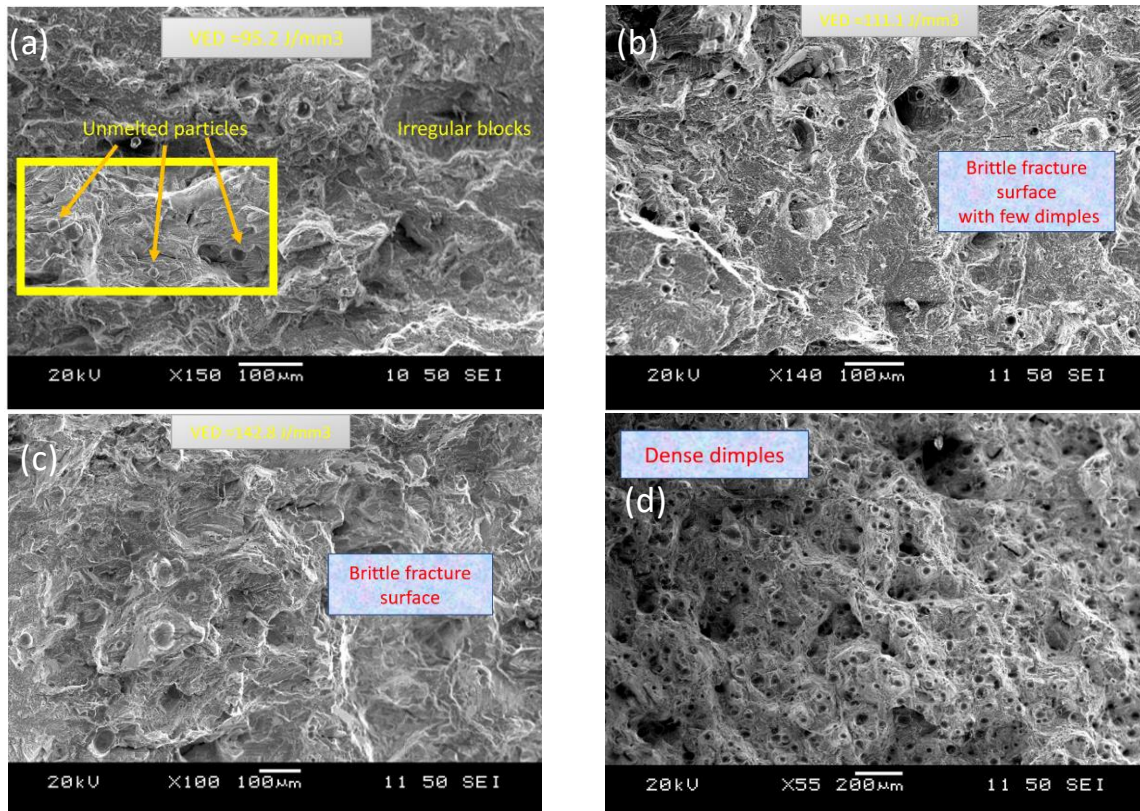


Figure 11. Fracture morphologies under different processing parameters. (a) TiC-IN738LC with VED=95.2 J/mm³ with magnified region inside; (b) TiC-IN738LC with VED=111.1 J/mm³; (c) TiC-IN738LC with VED=142.8 J/mm³; and d) IN738LC.

3.4. The strengthening mechanisms of nano-TiC particles

The anisotropic nature of materials by the L-PBF process is often reflected by the grain shape and size. Figure 12 shows the EBSD data of the IN738LC and TiC-IN738LC. As visible in Figure 12a, L-PBFed IN738LC alloy is characterized by elongated grains. An example of a completely different grain structure is shown in Figure. 12b: the alloy containing some TiC nanoparticles is indeed characterized by a fine distribution of the columnar grains, by impeding the grain boundary growth and forming the new nucleate sites. Figure. 12c and Figure. 12d show the grain size of pure IN738LC and TiC-IN738LC, and with the addition of the nano-TiC, the grain size is fully refined and much smaller than the pure IN738LC [40]. These nanoparticles prevent grain overgrowth and interfere with recrystallization. The occurrence of recrystallization is related to the accumulated internal strain energy. This energy exists in the form of dislocation density. Without recrystallization, large dendrites would remain and reduce mechanical properties [41].

According to the Hall-Petch formula, smaller grain sizes result in higher yield strengths [42]. The formula states that the yield strength of a polycrystalline material is inversely proportional to the square root of its grain size. Mathematically, the Hall-Petch formula can be expressed as:

$$\sigma_y = \sigma_0 + k_y d^{-\frac{1}{2}} \quad (2)$$

where σ_y is the yield strength of the material, σ_0 is the intrinsic strength of material, k_y is a constant term called the Hall-Petch slope and d is the average grain size of the material. According to the literature [43], the grain size strengthening $\Delta\sigma_y$ can be solved, with the lower limit 88 MPa to the upper limit 187 MPa, where in present work, the $\Delta\sigma_y$ is around 200 MPa and it slightly higher than the Hall-Petch method. Overall, the smaller grain size explains why the tensile strength is improved by the addition of the nano-TiC particles.

Figure 13 shows the schematics of nano-TiC reinforced IN738LC mechanism. When IN738LC powders are heated to high temperatures, the nanoparticles within them can impede the columnar growth and rearrange IN738LC matrix to form the smaller grains. One of the reasons is that nanoparticles can act as pinning sites for grain boundaries. Grain boundaries are the regions between individual grains, and they can be areas of high energy. When the IN738LC powders is heated, atoms can diffuse across grain boundaries and cause the grains to grow. However, if there are nano particles in the material, they can act as obstacles to this diffusion and grain boundary migration process, impeding grain growth [44]. Also, due to size of nano particles, they are typically much smaller than the grains themselves. When a material is heated, the larger grains will tend to grow at the expense of the smaller ones driven by interface energy. However, if there are nano particles present, they can act as nucleation sites for new grains, which can compete with the existing larger grains for material. This competition can impede the growth of the larger grains, leading to a finer microstructure [45].

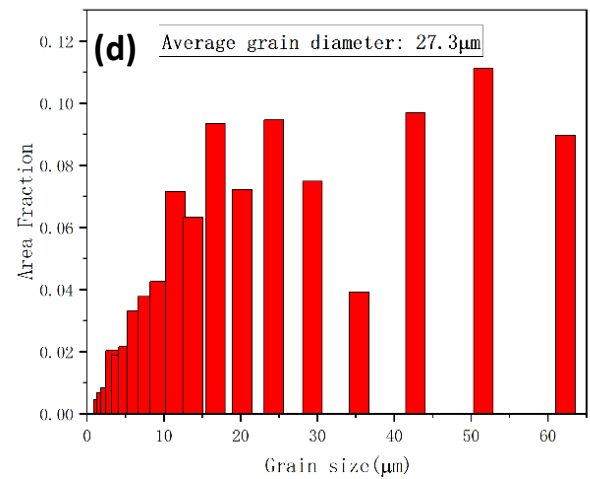
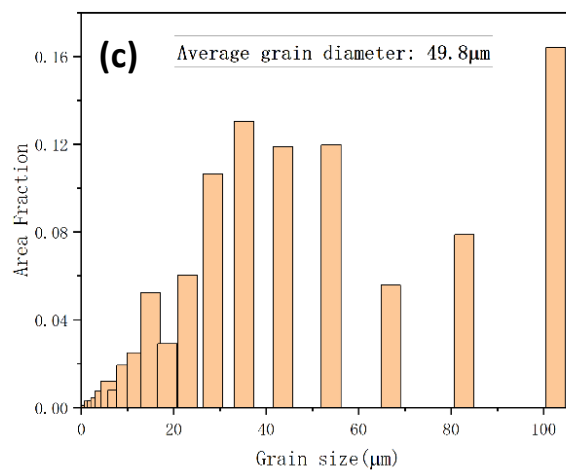
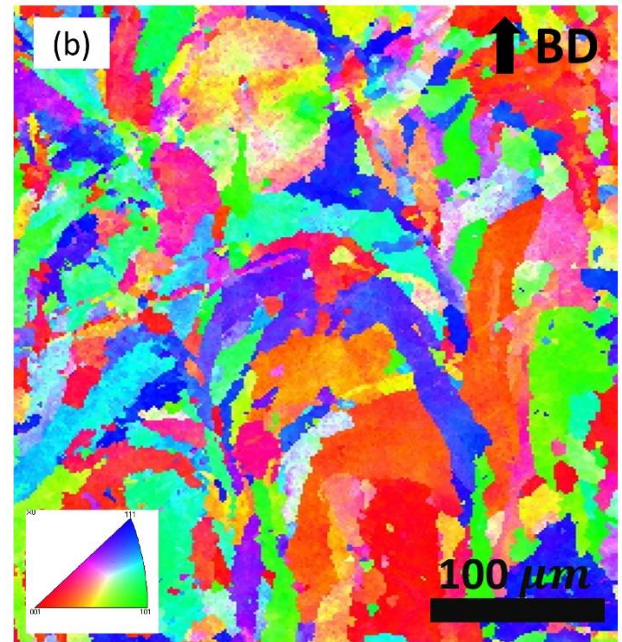
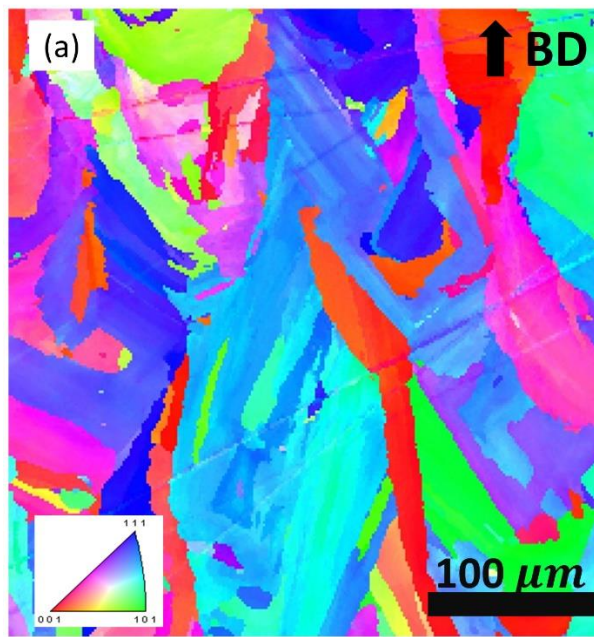


Figure 12. EBSD results of IN738LC and TiC-IN738LC composite: (a) IPF of IN738LC; (b) IPF of TiC modified IN738LC; (c) Grain size distribution graphs of pure IN738LC; (d) Grain size distribution graphs of TiC-IN738LC.

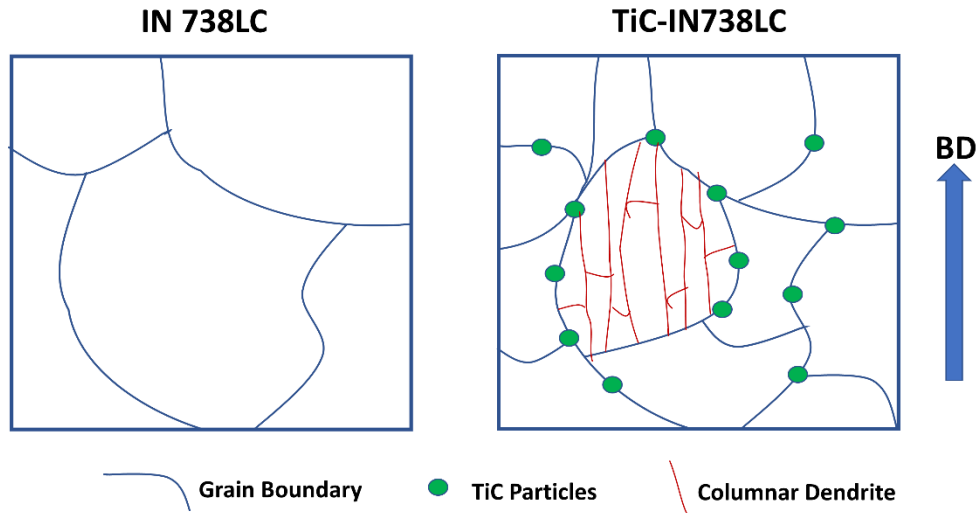


Figure 13. Schematic of nano-TiC reinforced IN738LC strengthening mechanism. The columnar dendrites are not shown on all the grains for the simplification.

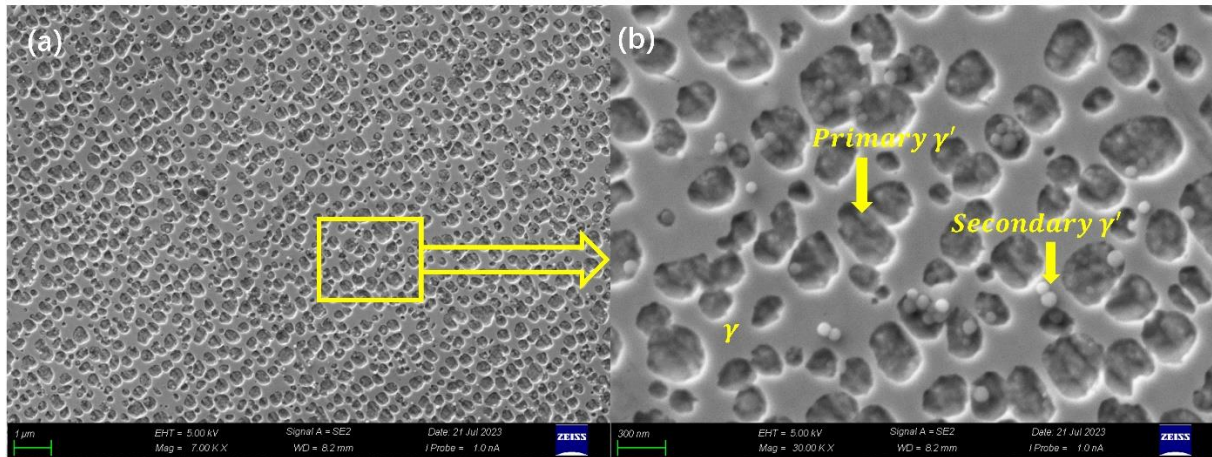


Figure 14. The microstructure of TiC-IN738LC. The primary γ' phase (cuboidal) and secondary γ' phase (spherical).

Figure 14 illustrates the microstructure of TiC-IN738LC, clearly depicting the presence of the γ' phase and the smaller secondary γ' precipitates. This observation substantiates the hypothesis that the introduction of nano-TiC nanoparticles does not obstruct the γ' phase generation, but rather augments its proliferation. The load-bearing strengthening mechanism is typically relevant to coherent precipitates, such as primary and secondary gamma prime (γ') phases, often observed in nickel-based superalloys [46]. The significant contribution of these γ' phases to the tensile strength of the material should be recognized. When subjected to external stress, the load distribution is facilitated between the material matrix and the precipitates. Owing to their intrinsic strength and stability, the precipitates effectively enhance the overall material strength by bearing a portion of the applied load. Essentially, these precipitates function as reinforcing elements within the matrix. The smaller secondary γ' precipitates play a pivotal role not only in load distribution but also in obstructing dislocation movement. The introduction of these precipitates increases the obstacle density that dislocations have to circumnavigate, resulting in additional strengthening. This process elevates the yield strength, which is instrumental in improving the overall tensile strength of the material.

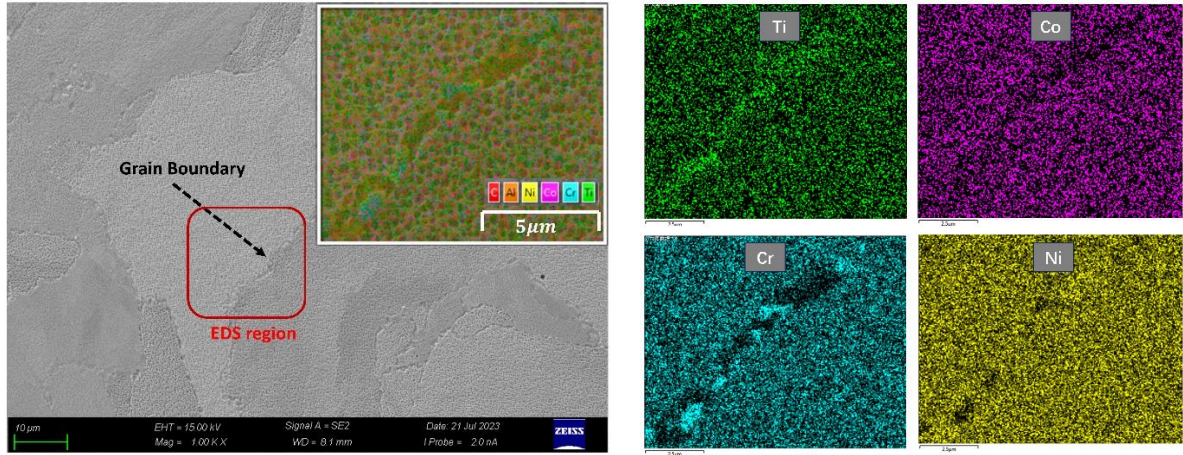


Figure 15. SEM/EDS of the TiC-IN738LC at the grain boundary region.

In Figure 15, EDS analysis was examined specifically in the grain boundary region. The analysis indicates a high concentration of Ti elements within this area, suggesting that the incorporation of TiC nanoparticles tends to accumulate at the grain boundary and the TiC nanoparticles function as impediments to dislocation movement. The EBSD result validates this observation, highlighting that the addition of these nanoparticles results in a significantly reduced average grain size compared to pure IN738LC. This phenomenon aligns with the Orowan strengthening mechanism, which posits that the creation of a dislocation loop around a nanoparticle demands more energy than navigating through an unobstructed lattice [47]. Consequently, the introduction of TiC nanoparticles increases the energy threshold required for the plastic deformation of the material. This increased energy requirement, in turn, amplifies the material's yield strength and hardness.

According to the experimental data, the processing parameters, which define the VED, correlate with the microhardness and tensile strength. From Figure 3 and Figure 7, at high scanning speeds, the obtained density and hardness are lower, which may be related to wettability and Rayleigh instability. The temperature of molten pool is calculated using Equation (3) below [48]:

$$T_{mp} = \frac{C_2}{\lambda \ln \left(\frac{C_1 S_S H_S}{L_P \lambda^5} + 1 \right)} \quad (3)$$

where C_1 and C_2 are the Planck's distribution constants, λ is the wavelength of the laser. Scanning speed is inversely proportional to melt pool temperature, and a higher scanning speed leads to a lower temperature and higher surface tension (according to the thermocapillary effect) [30,31]:

$$\gamma = \gamma^* \left(\frac{T_C - T_0}{T_C} \right) \left[1 - \left[\frac{C_2}{(T_C - T_0) \lambda \ln \left(\frac{C_1 S_S H_S}{L_P \lambda^5} + 1 \right)} - \frac{T_C - T_0}{T_C} \right] \right]^n \quad (4)$$

For Equation (4), γ^* is constant for each liquid, T_C is the critical temperature and T_0 is the reference temperature. Therefore, based on Equation (5), the surface tension values of the solid-liquid and liquid-gas phases are larger, increasing the chance of droplet generation [48-

50]. This phenomenon will lead to low wettability and an increasing chance of spheroidization, which is a common defect in metal AM and causes the porosity rate to increase and decrease the density and hardness [5, 48].

$$S = \gamma_{SG} - (\gamma_{SL} + \gamma_{LG});$$

$$\text{If } S > 0 \Rightarrow \text{Film appears} \quad (5)$$

$$\text{If } S < 0 \Rightarrow \text{Droplet appears};$$

Figures 3 and Figure 7 show that lower hardness and density were obtained with the lower input of laser power. According to Equation (3), less energy is transmitted to the molten pool at the lower laser power and the temperature of the molten pool is therefore decreased. In this case, due to the lack of the Marangoni convection, causing the higher heat penetration and generating more steam and bubbles within the molten pool. The bubbles tend to escape from the molten pool, and the interaction of steam forces with the hydrostatic pressure and surface tension will result in the formation of small pores and eventually weaken hardness properties. The steam force is directly related to the diameter of the pores. In a smaller diameter pore, the larger pressure on the pores results in larger forces, the steam tends to move to the top surface of the molten pool to escape and overcome the hydrostatic pressure as well as the surface tension, thus the keyhole is formed. Furtherly, this leads to the lack of fusion and the creation of large pores, even the cracks, thereby lowering the mechanical properties [5]. The morphology of the melt pool and grain structure are significantly affected Under different VED. A higher VED results in a deeper and wider melt pool, while a lower VED leads to a shallower and narrower one. The flow and spread of the powder also depend on VED. Differences in crystallization rates influence the distribution of TiC at grain boundaries, which directly relates to the material's mechanical and thermal properties. In summary, as stated above, the quality of an as-printed sample has a close relationship with the processing parameters, and research on optimizing the processing parameters and obtaining the correlations with microstructural data will gain a comprehensive understanding of material properties during the L-PBF process.

In this work, it can be concluded that cracks can be effectively suppressed by adding nano-ceramic particles. There are two main mechanisms for crack formation: liquefaction of low-melting phases and structural liquefaction[50, 51]. Carbides in the heat-affected zone have been considered as the primary phase which causes the structural liquefaction [52]. During the L-PBF, the thermal cycling of carbides can be very intense. However, due to the large temperature gradient and fast cooling rate, carbides do not have enough time to dissolve into the surrounding matrix. It has been clarified in previous studies that even introducing the higher carbon content, no liquid film was found at the interface between the carbide and the matrix by the characterization, namely no cracks caused by the structural liquefaction were observed. Similar findings were found in these studies [50, 51], which the tendency of structural liquefaction is a strong function of the carbide size. In this study, the TiC particles are the size of 50 nm, therefore, by the addition of the nano-TiC particles will benefit to mitigate the liquefaction effect and reduce the cracks.

4. Conclusion

This paper proposes a method of adding 2wt% nano- TiC particles to fabricate the IN738LC via L-PBF and the crack-free samples were achieved. The relationship between the processing parameters and the quality of as-printed samples was studied. Based on the nano-TiC strengthening principle, combined with the results from fracture morphology and mechanical tests, the mechanisms of obtaining high-quality TiC-IN738LC were theoretically described. The main conclusions of this study can be summarized as follows:

(1). The effects of process parameters on the density, porosity, hardness and tensile strength of nano-TiC reinforced IN738LC were comprehensively examined, and by optimizing the parameters, high-strength TiC-IN738LC could be prepared.

(2). The optimal parameters of high-density and low-porosity L-PBFed TiC-IN738LC are laser energy 225W, scanning speed 750mm/s, hatch spacing 0.09mm, and powder layer thickness 0.03mm.

(3). By adding TiC nanoparticle to IN738LC, a low-porosity and high-strength TiC-IN738LC was fabricated; Compared with the L-PBFed IN738LC, the microhardness of TiC-IN738LC increased by 20%-40%, and the tensile strength of TiC-IN738LC improved by 10%-30%. The synergistic effect of fine grain strengthening mechanism, load-bearing strengthening mechanism and Orowan strengthening mechanism was accounted for the performance enhancement.

(4). The results in this work provide an experimental reference for the L-PBF parameters of TiC-IN738LC, and furtherly expand the applications in terms of metal matrix composite in the fields of aerospace and deep-ocean exploration.

Acknowledgements

This work was supported by the National Natural Science Foundation of China [Grant number 51975301], Natural Science Foundation of Zhejiang, China [Grant number LZ22E050002] and the University of Birmingham that provided the funding.

Reference

1. Sanchez, S., et al., *Powder Bed Fusion of nickel-based superalloys: A review*. International Journal of Machine Tools and Manufacture, 2021. **165**<https://doi.org/10.1016/j.ijmachtools.2021.103729>.
2. Shi, J. and Y. Wang, *Development of metal matrix composites by laser-assisted additive manufacturing technologies: a review*. Journal of Materials Science, 2020. **55**(23): p. 9883-9917 <https://doi.org/10.1007/s10853-020-04730-3>.
3. Han, Q., et al., *Laser powder bed fusion of WC-reinforced Hastelloy-X composite: microstructure and mechanical properties*. Journal of Materials Science, 2020. **56**(2): p. 1768-1782 <https://doi.org/10.1007/s10853-020-05327-6>.
4. Chen, L., et al., *Microstructure evolution, mechanical properties, and strengthening mechanism of TiC reinforced Inconel 625 nanocomposites fabricated by selective laser melting*. Materials Science and Engineering: A, 2020. **792**<https://doi.org/10.1016/j.msea.2020.139655>.
5. Khorasani, A., et al., *The effect of SLM process parameters on density, hardness, tensile strength and surface quality of Ti-6Al-4V*. Additive Manufacturing, 2019. **25**: p. 176-186 <https://doi.org/10.1016/j.addma.2018.09.002>.
6. Tucho, W.M., et al., *Investigation of effects of process parameters on microstructure and hardness of SLM manufactured SS316L*. Journal of Alloys and Compounds, 2018. **740**: p. 910-925 <https://doi.org/10.1016/j.jallcom.2018.01.098>.
7. Kasperovich, G., et al., *Correlation between porosity and processing parameters in TiAl6V4 produced by selective laser melting*. Materials & Design, 2016. **105**: p. 160-170 <https://doi.org/10.1016/j.matdes.2016.05.070>.
8. Wang, H., et al., *Selective laser melting of the hard-to-weld IN738LC superalloy: Efforts to mitigate defects and the resultant microstructural and mechanical properties*. Journal of Alloys and Compounds, 2019. **807**<https://doi.org/10.1016/j.jallcom.2019.151662>.
9. Lv, Y., et al., *Cracking inhibition behavior and the strengthening effect of TiC particles on the CM247LC superalloy prepared by selective laser melting*. Materials Science and Engineering: A, 2022. **858**<https://doi.org/10.1016/j.msea.2022.144119>.
10. Ogunbiyi, O.F., et al., *Microstructural characteristics and thermophysical properties of spark plasma sintered Inconel 738LC*. The International Journal of Advanced Manufacturing Technology, 2019. **104**(1-4): p. 1425-1436 <https://doi.org/10.1007/s00170-019-03983-w>.
11. Lemos, G., et al., *Creep resistance improvement of a polycrystalline Ni-based superalloy via TiC particles reinforcement*. Materials Science and Engineering: A, 2022. **854**<https://doi.org/10.1016/j.msea.2022.143821>.
12. Wang, R., et al., *Novel selective laser melting processed in-situ TiC particle-reinforced Ni matrix composite with excellent processability and mechanical properties*. Materials Science and Engineering: A, 2020. **797**<https://doi.org/10.1016/j.msea.2020.140145>.
13. Zhou, W., et al., *Inhibition of cracking by grain boundary modification in a non-weldable nickel-based superalloy processed by laser powder bed fusion*. Materials Science and Engineering: A, 2020. **791**<https://doi.org/10.1016/j.msea.2020.139745>.
14. Gu, D., et al., *Laser additive manufacturing of nano-TiC reinforced Ni-based nanocomposites with tailored microstructure and performance*. Composites Part B: Engineering, 2019. **163**: p. 585-597 <https://doi.org/10.1016/j.compositesb.2018.12.146>.
15. Jia, Q. and D. Gu, *Selective laser melting additive manufacturing of TiC/Inconel 718 bulk-form nanocomposites: Densification, microstructure, and performance*. Journal of Materials Research, 2014. **29**(17): p. 1960-1969 <https://doi.org/10.1557/jmr.2014.130>.

16. Rong, T., et al., *Effects of tailored gradient interface on wear properties of WC/Inconel 718 composites using selective laser melting*. Surface and Coatings Technology, 2016. **307**: p. 418-427<https://doi.org/10.1016/j.surfcoat.2016.09.011>.
17. Zhang, B., et al., *Comparison of carbon-based reinforcement on laser aided additive manufacturing Inconel 625 composites*. Applied Surface Science, 2019. **490**: p. 522-534<https://doi.org/10.1016/j.apsusc.2019.06.008>.
18. Zhang, B., et al., *Microstructure and mechanical properties of Inconel 625/nano-TiB2 composite fabricated by LAAM*. Materials & Design, 2016. **111**: p. 70-79<https://doi.org/10.1016/j.matdes.2016.08.078>.
19. Zhang, H., et al., *Understanding tensile and creep properties of WC reinforced nickel-based composites fabricated by selective laser melting*. Materials Science and Engineering: A, 2021. **802**<https://doi.org/10.1016/j.msea.2020.140431>.
20. Mishurova, T., et al., *New aspects about the search for the most relevant parameters optimizing SLM materials*. Additive Manufacturing, 2019. **25**: p. 325-334<https://doi.org/10.1016/j.addma.2018.11.023>.
21. Koutiri, I., et al., *Influence of SLM process parameters on the surface finish, porosity rate and fatigue behavior of as-built Inconel 625 parts*. Journal of Materials Processing Technology, 2018. **255**: p. 536-546<https://doi.org/10.1016/j.jmatprotec.2017.12.043>.
22. Zhang, S., et al., *An experimental study of tensile property variability in selective laser melting*. Journal of Manufacturing Processes, 2019. **43**: p. 26-35<https://doi.org/10.1016/j.jmapro.2019.03.045>.
23. Majeed, A., et al., *Investigation of T4 and T6 heat treatment influences on relative density and porosity of AlSi10Mg alloy components manufactured by SLM*. Computers & Industrial Engineering, 2020. **139**<https://doi.org/10.1016/j.cie.2019.106194>.
24. Damon, J., et al., *Process dependent porosity and the influence of shot peening on porosity morphology regarding selective laser melted AlSi10Mg parts*. Additive Manufacturing, 2018. **20**: p. 77-89<https://doi.org/10.1016/j.addma.2018.01.001>.
25. Al-Maharma, A.Y., S.P. Patil, and B. Markert, *Effects of porosity on the mechanical properties of additively manufactured components: A critical review*. Materials Research Express, 2020. **7**(12): p. 122001<https://doi.org/10.1088/2053-1591/abcc5d>.
26. Hu, Y. and W. Cong, *A review on laser deposition-additive manufacturing of ceramics and ceramic reinforced metal matrix composites*. Ceramics International, 2018. **44**(17): p. 20599-20612<https://doi.org/10.1016/j.ceramint.2018.08.083>.
27. Webster, S., et al., *Physical mechanisms in hybrid additive manufacturing: A process design framework*. Journal of Materials Processing Technology, 2021. **291**: p. 117048<https://doi.org/10.1016/j.jmatprotec.2021.117048>.
28. Brennan, M., J. Keist, and T. Palmer, *Defects in metal additive manufacturing processes*. Journal of Materials Engineering and Performance, 2021. **30**(7): p. 4808-4818<https://doi.org/10.1007/s11665-021-05919-6>.
29. Fu, J., et al., *Multi-scale defects in powder-based additively manufactured metals and alloys*. Journal of Materials Science & Technology, 2022<https://doi.org/10.1016/j.jmst.2022.02.015>.
30. Khairallah, S.A., et al., *Laser powder-bed fusion additive manufacturing: Physics of complex melt flow and formation mechanisms of pores, spatter, and denudation zones*. Acta Materialia, 2016. **108**: p. 36-45<https://doi.org/10.1016/j.actamat.2016.02.014>.
31. Mohd Yusuf, S., et al., *Investigation on porosity and microhardness of 316L stainless steel fabricated by selective laser melting*. Metals, 2017. **7**(2): p. 64<https://doi.org/10.3390/met7020064>.
32. Wang, X., et al., *Microstructure and yield strength of SLM-fabricated CM247LC Ni-Superalloy*. Acta Materialia, 2017. **128**: p. 87-95<https://doi.org/10.1016/j.actamat.2017.02.007>.

33. Bi, G., et al., *Microstructure and tensile properties of superalloy IN100 fabricated by micro-laser aided additive manufacturing*. Materials & Design, 2014. **60**: p. 401-408<https://doi.org/10.1016/j.matdes.2014.04.020>.
34. Li, Y., et al., *Microstructures and mechanical properties evolution of IN939 alloy during electron beam selective melting process*. Journal of Alloys and Compounds, 2021. **883**: p. 160934<https://doi.org/10.1016/j.jallcom.2021.160934>.
35. Perevoshchikova, N., et al., *Optimisation of selective laser melting parameters for the Ni-based superalloy IN-738 LC using Doehlert's design*. Rapid Prototyping Journal, 2017. **23**(5): p. 881-892<https://doi.org/10.1108/RPJ-04-2016-0063>.
36. Yu, Z., et al., *The effect of Hf on solidification cracking inhibition of IN738LC processed by Selective Laser Melting*. Materials Science and Engineering: A, 2021. **804**: p. 140733<https://doi.org/10.1016/j.msea.2021.140733>.
37. Wei, S., et al., *Competitive failure analysis on tensile fracture of laser-deposited material for martensitic stainless steel*. Materials & Design, 2017. **118**: p. 1-10<https://doi.org/10.1016/j.matdes.2017.01.014>.
38. Yadollahi, A., et al., *Effects of process time interval and heat treatment on the mechanical and microstructural properties of direct laser deposited 316L stainless steel*. Materials Science and Engineering: A, 2015. **644**: p. 171-183<https://doi.org/10.1016/j.msea.2015.07.056>.
39. Li, P., et al., *Tensile fracture behavior of 316L stainless steel components fabricated with hybrid directed energy deposition and thermal milling manufacturing*. Applied Physics A, 2021. **127**(3): p. 1-10<https://doi.org/10.1007/s00339-021-04381-4>.
40. Fiocchi, J., A. Tuissi, and C. Biffi, *Heat treatment of aluminium alloys produced by laser powder bed fusion: A review*. Materials & Design, 2021. **204**: p. 109651<https://doi.org/10.1016/j.matdes.2021.109651>.
41. Godec, M., et al., *Hybrid additive manufacturing of Inconel 718 for future space applications*. Materials Characterization, 2021. **172**: p. 110842<https://doi.org/10.1016/j.matchar.2020.110842>.
42. Zhang, S., et al., *Graphene/ZrO₂/aluminum alloy composite with enhanced strength and ductility fabricated by laser powder bed fusion*. Journal of Alloys and Compounds, 2022. **910**: p. 164941<https://doi.org/10.1016/j.jallcom.2022.164941>.
43. Chen, Z., et al., *Graphene reinforced nickel-based superalloy composites fabricated by additive manufacturing*. Materials Science and Engineering: A, 2020. **769**: p. 138484<https://doi.org/10.1016/j.msea.2019.138484>.
44. Hansen, N., *Hall–Petch relation and boundary strengthening*. Scripta materialia, 2004. **51**(8): p. 801-806<https://doi.org/10.1016/j.scriptamat.2004.06.002>.
45. El-Awady, J.A., *Unravelling the physics of size-dependent dislocation-mediated plasticity*. Nature communications, 2015. **6**(1): p. 5926<https://doi.org/10.1038/ncomms6926>.
46. Zhang, Z., et al., *Microstructure and mechanical properties of ultrafine grained CoCrFeNi and CoCrFeNiAl_{0.3} high entropy alloys reinforced with Cr₂O₃/ Al₂O₃ nanoparticles*. Materials Science and Engineering a-Structural Materials Properties Microstructure and Processing, 2021. **816**<https://doi.org/10.1016/j.msea.2021.141313>.
47. Coakley, J., et al., *Lattice parameter misfit evolution during creep of a cobalt-based superalloy single crystal with cuboidal and rafted gamma-prime microstructures*. Acta Materialia, 2017. **136**: p. 118-125<https://doi.org/10.1016/j.actamat.2017.06.025>.
48. Khorasani, A.M., I. Gibson, and A.R. Ghaderi, *Rheological characterization of process parameters influence on surface quality of Ti-6Al-4V parts manufactured by selective laser melting*. The International Journal of Advanced Manufacturing Technology, 2018. **97**(9): p. 3761-3775<https://doi.org/10.1007/s00170-018-2168-6>.

49. Tian, Y., et al., *Influences of processing parameters on surface roughness of Hastelloy X produced by selective laser melting*. Additive Manufacturing, 2017. **13**: p. 103-112<https://doi.org/10.1016/j.addma.2016.10.010>.
50. Zhong, M., et al., *Boundary liquation and interface cracking characterization in laser deposition of Inconel 738 on directionally solidified Ni-based superalloy*. Scripta materialia, 2005. **53**(2): p. 159-164<https://doi.org/10.1016/j.scriptamat.2005.03.047>.
51. Zhou, W., et al., *Effect of carbon content on the microstructure, tensile properties and cracking susceptibility of IN738 superalloy processed by laser powder bed fusion*. Additive Manufacturing, 2022. **58**: p. 103016<https://doi.org/10.1016/j.addma.2022.103016>.
52. Dye, D., O. Hunziker, and R. Reed, *Numerical analysis of the weldability of superalloys*. Acta materialia, 2001. **49**(4): p. 683-697[https://doi.org/10.1016/S1359-6454\(00\)00361-X](https://doi.org/10.1016/S1359-6454(00)00361-X).